This is an open access article published under a Creative Commons Non-Commercial No Derivative Works (CC-BY-NC-ND) Attribution License, which permits copying and redistribution of the article, and creation of adaptations, all for non-commercial purposes.

LANGMUIR

Article

pubs.acs.org/Langmuir

Ostwald Ripening Growth Mechanism of Gold Nanotriangles in Vesicular Template Phases

Ferenc Liebig,[†] Andreas F. Thünemann,[‡] and Joachim Koetz*[,†]

[†]Institut für Chemie, Universität Potsdam, Karl-Liebknecht-Strasse 24-25, Haus 25, 14476 Potsdam, Golm, Germany

[‡]Bundesanstalt für Materialforschung und -prüfung (BAM), Unter den Eichen 87, 12205 Berlin, Germany

ABSTRACT: The mechanism of nanotriangle formation in multivesicular vesicles (MMV) is investigated by using time-dependent SAXS measurements in combination with UV−vis spectroscopy, light, and transmission electron microscopy. In the first time period 6.5 nm sized spherical gold nanoparticles are formed inside of the vesicles, which build up soft nanoparticle aggregates. In situ SAXS experiments show a linear increase of the volume and molar mass of nanotriangles in the second time period. The volume growth rate of the triangles is 16.1 nm^3/min, and the growth rate in the vertical direction is only 0.02 nm/min. Therefore, flat nanotriangles with a thickness of 7 nm and a diameter of 23 nm are formed. This process can be described by a diffusion-limited Ostwald ripening growth mechanism. TEM micrographs visualize soft coral-like structures with thin nanoplatelets at the periphery of the aggregates, which disaggregate in the third time period into nanotriangles and spherical particles. The 16 times faster growth of nanotriangles in the lateral than that in the vertical direction is related to the adsorption of symmetry breaking components, i.e., AOT and the polyampholyte PalPhBisCarb, on the {111} facets of the gold nanoplatelets in combination with confinement effects of the vesicular template phase.

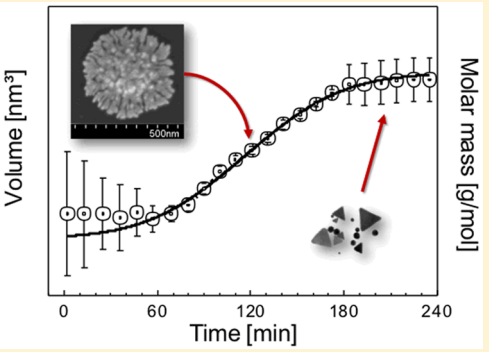

1. INTRODUCTION

Asymmetric-shaped gold nanocrystals are of increasing interest due to their shape-dependent optical properties.[1−3] Recently, we have shown promising results of gold nanotriangles in surface-enhanced Raman scattering,[4] in good agreement with earlier published data from Scarabelli et al.[5] Flat nanotriangles exhibit a more intensive longitudinal absorption band in the UV−vis spectra between 700 and 1400 nm (in-plane surface plasmon absorption band in the near-infrared (NIR) region).[6] The absorption maximum in the NIR region can be tuned by controlling the size and thickness of the individual nanotriangles,[7,8] which is of major biological importance for imaging applications in tissue[9] or hyperthermia of cancer cells.[10]

Unlike in the case of anisotropic gold nanorods where the seed-mediated synthesis is mainly accepted,[1,3,11,12] the mechanism of nanotriangle formation is under debate. The growth of very small, preformed spherical gold seeds into anisotropic nanoparticles requires symmetry-breaking components, e.g., cationic surfactants like CTAB.[13] However, the anisotropic nanocrystal growth can be influenced by a specific addition of halide ions[14,15] or by changing the kinetic conditions.[16] Therefore, the crystallization process can lead to rod-shaped or platelet structures. At a slow reaction rate in the presence of iodide ions predominantly nanotriangles are formed in such seed-mediated synthesis.[16]

Furthermore, gold nanotriangles can be synthesized by adding shape-controlling agents, e.g., lemon grass extracts[2] or tryptophan,[17] as well as in template phases, e.g., dendrimers or block copolymer micelles can take over this role.[18,19] Ding et al. used amphiphilic block copolymer micelles as templates to direct the formation of triangular $CuCl_2$ prisms.[19] The oriented mineralization process of $CuCl_2$ nanotriangles in such template phases is discussed through the spatial confinement from block copolymer micelles.

Our own research activities in this field were focused on the one-step synthesis of nanotriangles in the presence of vesicles. Robertson et al. already observed that in the presence of mixed SDS/phospholipid vesicles extra-long nanorods and nanotriangles are formed.[20] The amount of nanotriangles can be increased by adding a maltose-modified polyethylenimine (malPEI).[21] Recently performed experiments with AOT/phospholipid based vesicles in the presence of a polyampholyte, i.e., PalPhBisCarb, show that under optimized conditions the amount of anisotropic particles can yield 60% and the corresponding amount of nanotriangles 30%.[4,7] Noteworthy, also the seed-mediated synthesis leads only to a shape yield of nanotriangles of about 50%.[5] Therefore, in all cases an additional separation step, e.g., depletion flocculation, is necessary to isolate and purify gold nanotriangles.[4,5] In the present work we performed time-dependent experiments to investigate the nanotriangle formation process in the presence of the vesicular template phase. By using different methods, i.e., UV−vis spectroscopy, light microscopy (LM), transmission electron microscopy (TEM) in combination with SAXS measurements,

Received: July 19, 2016
Revised: September 7, 2016
Published: October 3, 2016

 © 2016 American Chemical Society

DOI: 10.1021/acs.langmuir.6b02662
Langmuir 2016, 32, 10928−10935

the crystal growth process is investigated on the time scale. The nanoparticle formation process can be divided into three periods. First, only spherical particles are formed, whereas in the second period flat gold platelets grow up at the periphery of soft particle aggregates. This process can be described by Ostwald ripening. Particle aggregate decomposition proceeds in the third period.

2. EXPERIMENTAL SECTION

2.1. Chemicals. The surfactant dioctyl sodium sulfosuccinate (AOT) with a purity of 98% and tetrachloroauric(III) acid ($HAuCl_4 \cdot 3H_2O$) were purchased from Sigma-Aldrich. The phospholipid PL90G (purity > 97.3%) was obtained from PHOSPHOLIPID GmbH. The strongly alternating copolymer poly(*N*,*N*′-diallyl-*N*,*N*′-dimethylammonium-*alt*-3,5-bis-carboxyphenyl-maleamic carboxylate) (PalPhBisCarb) was synthesized by free radical polymerization according to the procedure described by Fechner and Koetz.[22] The molecular weight (15 000 g/mol) was estimated viscometrically by using available constants of the homopolymer poly(diallyldimethylammonium chloride) (PDADMAC) for the Kuhn−Mark−Houwink−Sakurada equation ($K = 1.12 \times 10^{-4}$ dL g^{-1}, $\alpha = 0.82$ in 1 M NaCl at 25 °C). Only Milli-Q Reference A+ water was used in all of the described experiments.

2.2. Methods. UV−vis absorption measurements were performed with an Agilent 8453 UV−vis−NIR spectrometer in wavelengths between 200 and 1100 nm. Shape and size of the gold nanoparticles were determined by transmission electron microscopy (TEM). To realize the time-dependent measurements every 30 min 3 μL of the sample was taken out, dropped on carbon-coated copper grids, and fast dried by removing the excess liquid with filter paper. Subsequently, the samples were examined using the JEM-1011 (JEOL, Japan) at an acceleration voltage of 80 kV. In addition to TEM, a Hitachi S-4800 scanning electron microscope (SEM) was used. Therefore, the sample was shock frozen by plunging into nitrogen slush at atmospheric pressure and afterward freeze fractured at −180 °C, etched for 45 s at −98 °C, and sputtered with platinum in the GATAN Alto 2500-S cryo-preparation chamber to expose the inner structure of the vesicles. In order to obtain the zeta potential, the Malvern Nano Zetasizer 3600, based on the principle of electrophoretic light scattering, was employed.

SAXS measurements were performed in a flow-through capillary with a Kratky-type instrument (SAXSess from Anton Paar, Austria) at 21 ± 1 °C. The SAXSess has a low sample-to-detector distance of 0.309 m, which is appropriate for investigation of dispersions with low scattering intensities. The measured intensity was converted to absolute scale according to Orthaber et al.[23] The scattering vector is defined in terms of the scattering angle q and the wavelength of the radiation (λ = 0.154 nm): thus, $q = 4\pi n/\lambda \sin\theta$. Deconvolution (slit length desmearing) of the SAXS curves was performed with the SAXS-Quant software. Samples analyzed with SAXS were used as prepared. Curve fitting was conducted with software SASfit for determination of particles size parameters and volume fraction.[24] The reference material RM 8012 from NIST containing gold nanoparticles with a nominal diameter of 30 nm and a gold concentration of 48.17 ± 0.33 μg g^{-1} was used as quality control material.[25]

3. RESULTS AND DISCUSSION

3.1. Template Phase Characterization. DLS experiments of the turbid, aqueous AOT/phospholipid mixture, used as a template phase for gold nanoparticle formation, show a very broad size distribution from small particles of about 50 nm up to very large particles in the micrometer size range, in full agreement with our recently published DLS data.[4] The corresponding zeta potential is −78 ± 2 mV. Control experiments of the AOT micelles exhibit a negative zeta potential of −106 ± 4 mV and of phospholipon vesicles of −17 ± 2 mV. Hence, the formation of mixed AOT/phospholipon vesicles (schematically shown by us already earlier[29]) can be assumed, reinforced by light microscopic investigations, which show small vesicular structures besides giant vesicles on the micrometer scale (compare Figure 2). For a more comprehensive characterization, additional cryo-SEM experiments were performed. In Figure 1 small unilamellar vesicles (SUV) and significantly larger giant vesicular structures, i.e., multivesicular vesicles (MVV), can be observed. The results confirm our recently published experiments.[4] Our freeze−fracture TEM micrographs have already shown that the reduction process to form gold nanoparticles starts at the surface of mixed small unilamellar vesicles (SUV).[20]

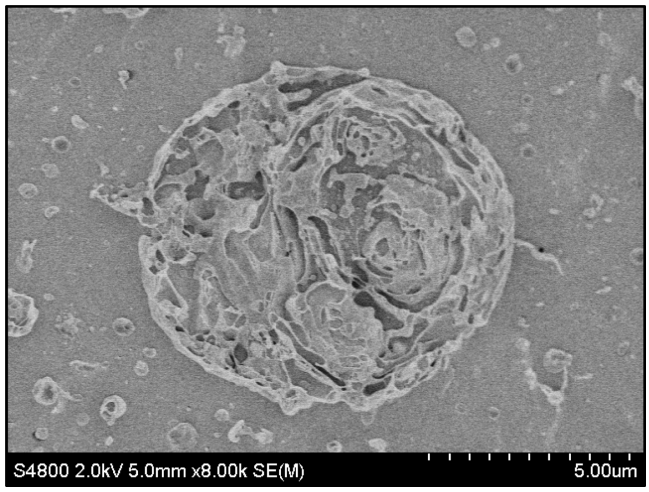

Figure 1. Cryo-SEM micrograph of small unilamellar (SUV) and giant multivesicular vesicles (MVV).

3.2. Reducing Behavior of the Components. Investigations of the reducing properties of the components show that only in the presence of PL90G/AOT mixed vesicles, gold nanotriangles are formed. Adding a polymer can influence the amount of triangles and the shape of the vesicles. AOT micelles show no reducing effects in aqueous solution but have interesting effects on crystal growth.[26] In the case of an aqueous phospholipid solution only spherical particles are formed. This is in agreement with other authors using vesicle templates for in situ reduction of metal nanoparticle precursors.[27,28] Recently, we have shown that the polyampholyte PalPhBisCarb can transform vesicles into tubular network structures after ultrasonic treatment.[29] Under the conditions used here a lot of junction points exist in the inner structure of the MVV (compare Figure 1) in similarity to tubular structures. However, PalPhBisCarb is not able to reduce the gold chloride solution alone. Recently performed control experiments have shown that in the absence of PalPhBisCarb nanotriangles are not formed at room temperature.[37] When PalPhBisCarb is added stepwise to the mixed template/tetrachloraureate solution at higher temperatures the amount of nanotriangles can be significantly increased. These experiments clearly show the symmetry-breaking effect of the polyampholyte.

3.3. Time-Dependent UV−vis Experiments in Combination with Light Microscopy and Transmission Electron Microscopy. To clarify the mechanism of nanotriangle formation different time-dependent experiments at room temperature were performed to characterize the sample by UV−vis spectroscopy, LM, and TEM microscopy. UV−vis absorption spectra permit a general and quickly accessible statement to the size and shape of the gold nanoparticles. The first sharper peak at about 530 nm can be assigned to the growth of spherical gold nanoparticles, and the broad peak from 700 to 1050 nm indicates the formation of anisotropic gold nano-

DOI: 10.1021/acs.langmuir.6b02662
Langmuir 2016, 32, 10928−10935

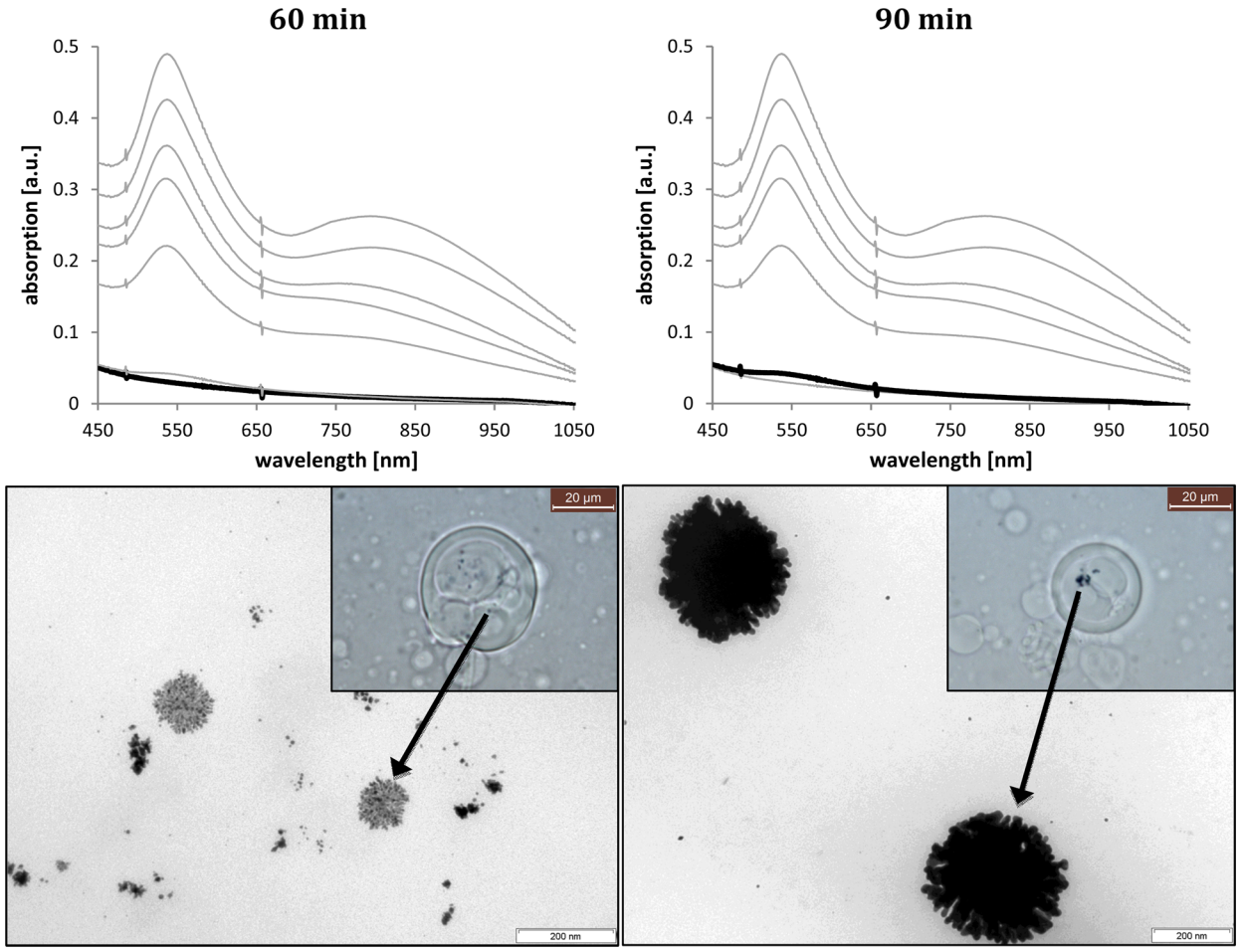

Figure 2. Analysis of the dispersion after 60 (left) and 90 min (right) by UV−vis (top), TEM (bottom), and light microscopy (inset).

particles. Both grow up in time (spectra from bottom to the top) as seen in Figures 2, 3, and 4. The time-relevant UV spectrum (after 60, 90, 120, 150, and 210 min) is marked in each figure with a black thick line. For a more detailed particle characterization TEM micrographs were performed. In addition, LM experiments offer the opportunity to fix the position in the template phase where the gold nanoparticle formation process starts, and SAXS measurements provide information about the reaction mechanism.

After 60 min small "points" can be observed inside of the multivesicular vesicles using the light microscope. TEM micrographs validate that these "points" in the LM micrograph are soft spherical aggregates of about 170 nm in size (Figure 2). Zooming in, these aggregates (compare Figure 10) are composed of very small nanoparticles. After 90 min the number of better-contrasted small "points" inside the vesicles is increased, as seen in Figure 2 (right). TEM micrographs show that the soft aggregates grow up to 300 nm. It has to be mentioned here that the TEM pictures are two-dimensional projections of three-dimensional aggregated objects. Therefore, the aggregate structures visibly appear more compact in the projection than they are in three dimensions. At the same time a broad UV−vis absorption peak (marked spectrum in Figure 2, right column) at about 550 nm becomes detectable, which can be related predominantly to the plasmon resonance peak of spherical gold nanoparticles. The TEM micrograph shows small platelets that are formed at the periphery of the aggregates. Similar aggregate structures were observed by precipitating octacalcium phosphate (OCP) crystal platelets in the presence of AOT.[26] That means AOT is of relevance for the asymmetric growth of individual nanoplatelets as well as the assembly to nanoplatelet aggregates.

As can be seen in the TEM micrograph, the individual platelets in the shell grow out of the core after 120 min to build up a coral-like structure with vertical plates radiating from the center. The corresponding UV−vis spectrum shows a second broad UV absorption peak at about 800 nm, indicating the formation of anisotropic nanoparticles.

In the next TEM micrograph, performed after 150 min, an onset of decomposition of the aggregates can be observed. This means that some of the aggregates become smaller and the individual platelets from the outer shell disaggregate. In consequence, the UV−vis absorption peak of asymmetric nanoplatelets is increased. At the same time the absorption band at 530 nm increases too, representing simultaneous formation of spherical gold nanoparticles. This process is accompanied by decomposition of the multivesicular vesicles. For that reason the turbid solution gets optically clear and becomes red colored due to the increasing amount of gold nanoparticles of different size and shape.

After 210 min the color change to red can also be seen outside of the multivesicular vesicles. The amount of MVV is decreased, and the inner structure of the MVV seems to dissipate slowly. The coral-like aggregate structures are extremely rare and small, and the gold nanoparticle formation process comes to an end.

DOI: 10.1021/acs.langmuir.6b02662
Langmuir 2016, 32, 10928−10935

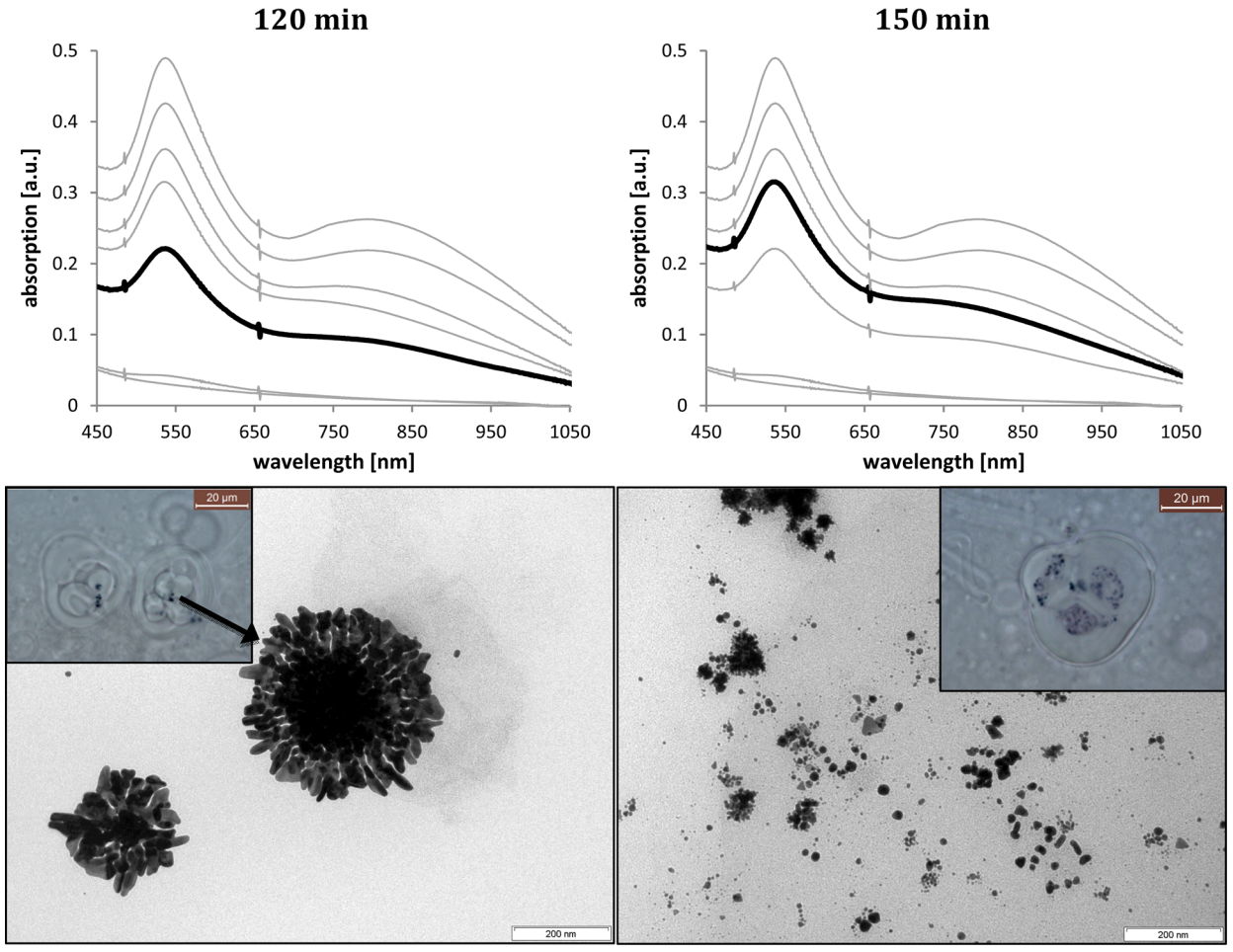

Figure 3. Analysis of the dispersion after 120 (left) and 150 min (right) by UV−vis (top), TEM (bottom), and light microscope (inset).

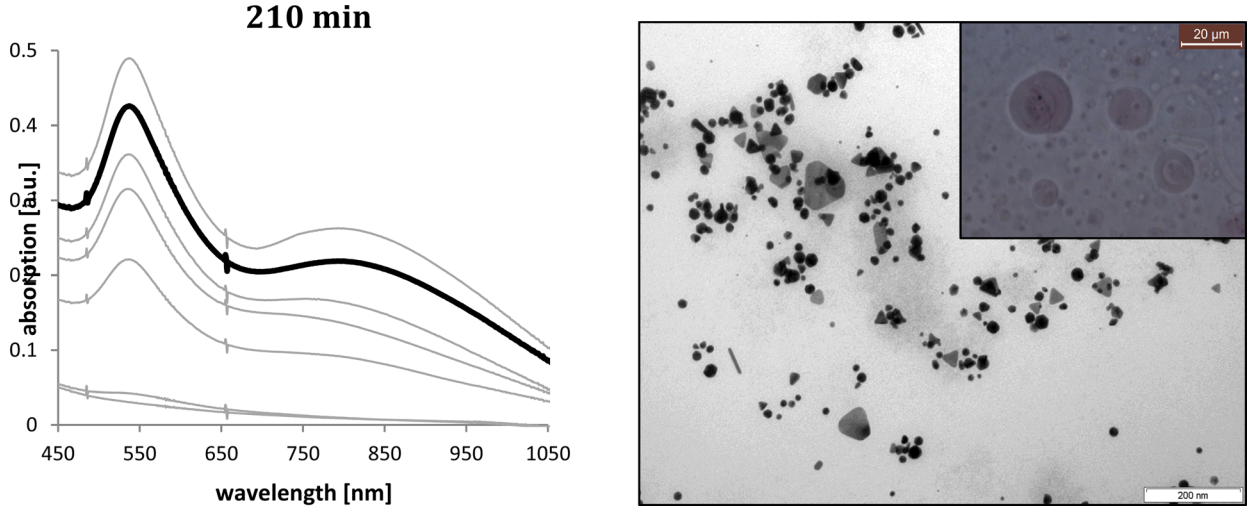

Figure 4. Analysis of the dispersion phase after 210 min by UV−vis (top), TEM (bottom), and light microscope (inset).

To underline the results obtained by UV−vis spectroscopy, LM, and TEM microscopy time-dependent SAXS measurements were performed.

3.4. Time-Dependent SAXS Experiments. The SAXS measurements were performed in situ, while the reaction proceeds with averaging time intervals of 10 min. The gold X-ray scattering contrast of 1.0596×10^{12} cm^{-2} is 3 orders of magnitude larger than that of the vesicles, and therefore, we "see" exclusively the gold particles. In other words, we "look" into the vesicles. Statistically significant ensemble averages of the scattering pattern were provided by an irradiated volume of 10 μL. Examples for the scattering profile at an early stage and at the end of the reaction are shown in Figure 5. For reaction times of $t \leq 60$ min the curves can be fitted by simple spheres with a radius of 6.5 ± 0.4 nm as shown in the upper inset of Figure 5. The shape of the scattering curves for reaction times larger than 60

DOI: 10.1021/acs.langmuir.6b02662
Langmuir 2016, 32, 10928−10935

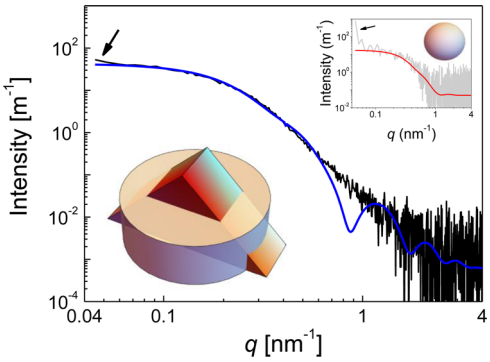

Figure 5. SAXS intensity as a function of the scattering vector and a curve fit of a nanodisk gold particle with a mean height of 7.1 ± 0.1 nm and a diameter of 23 ± 1 nm. Reaction time was t = 235 min. Lower inset shows a nanotriangle and a nanodisk with the same thickness and the same radius of gyration. Upper inset shows the scattering of a sphere with a radius of R = 6.5 ± 0.4 nm measured at t = 36 min. Arrows indicate the onset of increase of the scattering intensity due to aggregation.

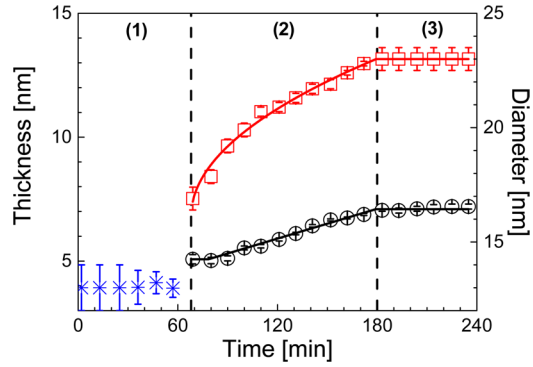

Figure 6. Particle size parameters as a function of the reaction time. Given are the mean diameter of spherical particles (blue crosses) at $t \leq$ 60 min (period 1). At later times thicknesses and diameters of plate-like particles are plotted (black circles and red squares, respectively) during nanotriangle growth at 60 min < t < 180 min (period 2) and as full-grown nanotriangles t > 180 min (period 3).

min cannot be interpreted in terms of spherical particles. For their interpretation we fitted the scattering curves with the model scattering function of a thin disk instead of a nanotriangle because the scattering function for the latter is not available for curve fits.[24] This simplified scattering model was found applicable over a wide q range for reaction times larger than 60 min. An example of measured and fitted curves, resulting in a mean particle thickness of 7.1 ± 0.1 nm and a mean diameter of 23 ± 1 nm, can be seen in Figure 5 (black and blue line, respectively). The reaction time was t = 235 min. The inset visualized the ideal nanotriangle and a disk with the same platelet thickness and the same radius of gyration as used for fitting. It is obvious that this disk model is oversimplified at large scattering vectors, but this is not critical for our interpretation. We did not include an analysis of polydispersity to avoid ambiguous results due to the danger of overfitting. An increase of the scattering intensity, where the data points lie above the model curves, is visible at q values lower that 0.05 nm^{-1}. This corresponds to distances larger than π/0.05 nm = 62 nm (see arrows in Figure 5) and indicates that effects of aggregation are not interfering with the particle scattering. Surprisingly, no structure factor needs to be taken into account. That means that the individual particles are already significantly separated from each other within loosely packed, soft aggregate structures shown in Figure 10. In contrast, for densely packed aggregates we must expect a much stronger increase of the scattering intensity with an early onset that interferes strongly with the particle form factor.

An overview of the particle size parameters as derived from the model fits is given in Figure 6. It can be seen there that the spherical particles display mean diameters of about 13 nm with relatively large uncertainties in period 1. Next, the thicknesses increases from 5.1 nm at t = 69 min to 7.5 nm at t = 183 min in period 2. Therein the diameters increase from 16.9 to 23.0 nm. At later times, in period 3, the size parameters are constant and the nanotriangles are full grown.

We quantified the volume of the particles as $V = 4/3\pi(\text{radii})^3$ in period 1 and as V = thickness × π(diameter)^2 in periods 2 and 3. The volumes are constant in period 1, increase linearly in period 2, and are again constant in period 3 as can be seen in Figure 7. We quantified this observation by

$$
\begin{aligned}
V(t) &= V_1 \qquad \text{for } t \leq t_{1,V} \\
V(t) &= b + m_V t \quad \text{for } t_{1,V} < t < t_{2,V} \\
V(t) &= V_2 \qquad \text{for } t \geq t_{2,V}
\end{aligned} \tag{1}
$$

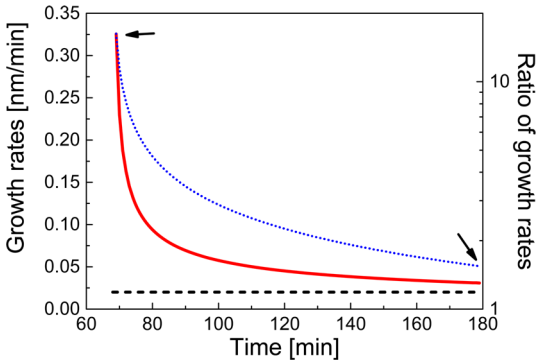

Figure 7. Growth rates of the thickness and diameter in period 2 (black dashed and red solid line, respectively). Growth rate of the thicknesses is $\dot{h}(t) = m_h = 0.020 \pm 0.001$ nm min^{-1}. The growth rate of the diameters is $\dot{d}(t) = k/(2\sqrt{t - t_{1,d}})$, with k = 0.651 ± 0.029 nm s$^{1/2}$ and $t_{1,d}$ = 68 ± 2. The ratio of the growth rates is $\dot{d}(t)/\dot{h}(t) = k/(2m_h\sqrt{t - t_{1,d}})$ (blue dotted line). This ratio decreases from 16 at t = 69 min to 1.5 at t = 179 min (indicated by arrows).

where m_V is the growth rate of the nanotriangle volumes, V_1 is the particle's volume when the triangles start to grow, and V_2 is the final volume of the triangles. The initial time for the first observation of the nanotriangles is $t_{1,V} = (V_1 - b)/m_V$, and they stopped growing at $t_{2,V} = (V_2 - b)/m_V$. The curve fit using eq 1 results in V_1 = 1163 ± 31 nm^3 and V_2 = 2960 ± 31 nm^3. Using this approach period 1 ends at $t_{1,V}$ = 68 ± 3 min and period 3 starts at $t_{2,V}$ = 180 ± 2 min. The volume growth rate of the nanotriangles is m_V = 16.1 ± 0.3 nm^3 min^{-1} in period 2.

Next, it is of interest how the thickness and the diameter of the nanotriangles contribute to the volume growth. The growth of the thickness in period 2 is linear, while the increase of the diameter is nonlinear as can be seen in Figure 6. Similar to eq 1 we quantified the nanoplate thickness as

DOI: 10.1021/acs.langmuir.6b02662
Langmuir 2016, 32, 10928−10935

$$h(t) = h_1 \quad \text{for } t \le t_{1,h}$$
$$h(t) = b_h + m_h t \quad \text{for } t_{1,h} < t < t_{2,h}$$
$$h(t) = h_2 \quad \text{for } t \ge t_{2,h} \tag{2}$$

The resultant fit as shown in Figure 6 (black solid line) results in an initial thickness of $h_1 = 5.1 \pm 0.3$ nm and a final thickness of $h_2 = 7.1 \pm 0.1$ nm. Period 1 ends at $t_{1,h} = 78 \pm 13$ min, and period 2 at $t_{2,h} = 180 \pm 2$ min. The growth rate of the thickness of the triangles is $m_h = 0.020 \pm 0.001$ nm min^{-1} in period 2.

Since the volume and thickness of the nanotriangles grow linear in period 2 it is straightforward that the diameters grow proportional to the square root of time. Therefore, we quantified the diameter as

$$d(t) = d_1 \quad \text{for } t \le t_{1,d}$$
$$d(t) = d_1 + k\sqrt{t - t_{1,d}} \quad \text{for } t_{1,d} < t < t_{2,d}$$
$$d(t) = d_2 \quad \text{for } t \ge t_{2,d} \tag{3}$$

The result of using eq 3 for interpretation of the diameter is shown in Figure 6 (red solid line). Using this approach, the initial time when the nanotriangles are first observed is $t_{1,d} = 68 \pm 2$. The end of the growth of the diameter is $t_{2,d} = t_{1,d} + (d_2 - d_1)^2/k^2$, 180 ± 5 min. The growth constant is $k = 0.651 \pm 0.029$ nm s$^{1/2}$.

Now we can compare the growth rate of the nanotriangles' thickness, $\dot{h}(t) = m_h$, with the growth rate of their diameter, $\dot{d}(t) = k/(2\sqrt{t - t_{1,d}})$, for times between $t_{1,d}$ and $t_{2,d}$. Figure 7 demonstrates that the growth rate of the diameter is at any time larger than the growth rate of the height (red solid and black dashed line, respectively). The ratio of the growth rates, $\dot{d}(t)/\dot{h}(t) = k/(2m_h\sqrt{t - t_{1,d}})$, allows a direct comparison (blue dotted line in Figure 7). Thus, the growth rate of the diameter is 16 times larger than that of the height at $t = 69$ min and decreases to 1.5 times at $t = 179$ min (indicated by arrows).

The volume fraction, $\phi(t)$ of the nanotriangles as a function of time were determined as described recently[24] and displayed in Figure 8. Since the volume increases linearly in phase 2 we quantified the time dependence of the volume fraction analogously to eq 1. The results are given in Figure 8.

For the volume fraction we found that period 1 ends at $t_{1,\phi} = 63 \pm 2$ min where the nanotriangle fraction is $\phi(t_{1,\phi}) = 0$. The volume fraction of triangles increases with a slope of $m_\phi = (1.09 \pm 0.04) \times 10^{-7}$ min^{-1} between $t_{1,\phi}$ and $t_{2,\phi}$. Period 3 begins at $t_{2,\phi} = 176 \pm 3$ min, where $\phi(t_{2,\phi}) = (1.24 \pm 0.04) \times 10^{-5}$. Multiplication of this final volume fraction with the bulk density of gold gives a nanotriangle gold concentration of 0.245 g L^{-1}. This is about 17% less than the total concentration of 0.295 g L^{-1} gold in the form of gold salt used for the synthesis. Therefore, we can estimate that about 83% of the gold is finally found in the nanotriangles.

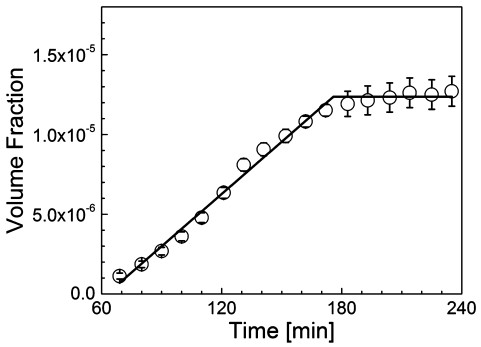

Figure 8. Volume fraction of the triangles as a function of reaction time. Solid lines are the corresponding curve fits.

Figure 9 shows the time-dependent increase of the volume and molar mass of the triangles. The linear increase in the mean particle volume with time can be described by a diffusion-limited Ostwald ripening.[30] Due to the decrease of supersaturation in a closed system, smaller crystals with a radius r below a critical value (r^*) must dissolve whereas larger crystals with $r > r^*$ must grow.[31] This process is thermodynamically preferred and can be explained for large particles by a mathematical approach, developed by Lifshitz, Slyozov, and Wagner.[32,33] In situ time-resolved SAXS measurements have shown that the growth of rhodium and palladium nanoparticles in an aqueous ethanol solution in the presence of PVP proceeded via an Ostwald ripening-based growth mechanism,[30] in contrast to gold nanoparticles.[34]

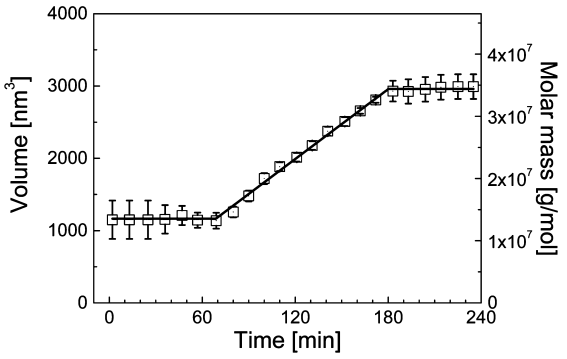

Figure 9. Mean volume of the particles as a function of time and corresponding curve fit (squares and solid line, respectively). Right axis is the molar mass of the triangles presuming the same density as gold in bulk state of 19.3 g/cm^3.

3.5. Growth Mechanism. On the basis of the results shown here the time-dependent gold nanotriangle formation process can be divided into different periods.

- Period I: 0−60 min. In the first hour the radius of the gold nanoparticles determined by SAXS is quite constant at 6.5 ± 0.4 nm, indicating that spherical particles are formed. These nanoparticles are formed at the bilayer of the mixed vesicles by a "classical" nucleation process. Inside of the multivesicular vesicles (compare Figure 1), where the number of junction points between the AOT/phospholipid bilayers is much higher in similarity to tubular networks,[29] the local concentration of individual formed gold nanoparticles is also increased. TEM micrographs, performed after 60 min, illustrate that these nanocrystallites build up soft particle aggregates of about 170 nm in size. It can be assumed that AOT plays an important role in the aggregation process, in analogy to the results shown by Bujan et al.[26] SDS shows similar effects,[26] which explains previously published results with SDS/phospholipon vesicles.[20]
- Period II: 60−180 min. SAXS measurements show that after 1 h flat nanocrystals are formed. The initial platelet thickness of 5.1 ± 0.3 nm is increased only marginally up to 7.1 ± 0.1 nm, whereas the nanotriangle diameter as well as the volume and molar mass (Figure 9) are increased

DOI: 10.1021/acs.langmuir.6b02662
Langmuir 2016, 32, 10928−10935

linearly. The growth rate in lateral direction is 16 times larger than in the vertical direction. This process can be well described by an Ostwald ripening-based growth of gold nanotriangles. Hereby the preliminary formed small nanocrystals with $r < r^*$ disappear, whereas the flat nanoplatelets in the periphery of the aggregates grow up to coral-like structures.

- Period III: 180−250 min. After 180 min the growing process is leveled off, resulting in constant nanotriangle diameter, volume, and molar mass. The TEM micrographs show that the particle aggregates decompose into nanotriangles and spherical particles.

The proposed mechanisms for the formation of energetically unfavorable anisotropic nanotriangles fall into two categories:

- by adding symmetry breaking compounds adsorbing to specific crystal faces
- by using template phases as space-confining structures.

In our case both mechanisms are of relevance, this means, the template effect of the vesicles and the preferential adsorption of capping agents, i.e., AOT and PalPhBisCarb.

Our recently published HRTEM investigations have shown that the nanotriangles exhibit very large {111} bottom and top faces and twin planes oriented parallel to the substrate plane with alternating concave and convex side faces.[7] Therefore, the growth in the lateral direction is preferred at the concave side faces according to the model proposed by Lofton and Sigmund.[35] AOT and PalPhBisCarb can bind selectively to {111} facets of the platelets and can thereby reduce the growth rate in the vertical direction.[36] Confinement effects in the coral-like aggregate structure (template effect) furthermore influence the growth of gold nanoplatelets subsequently proceeded via a diffusion-limited Ostwald ripening-based mechanism.

Figure 10 summarizes our results with regard to the time-dependent aggregate formation and decomposition.

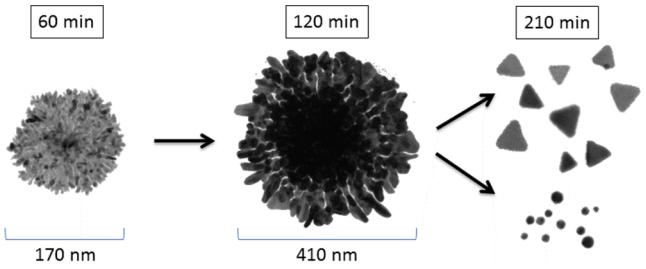

Figure 10. Time-dependent gold nanotriangle formation in a vesicular template phase.

4. CONCLUSIONS

Time-dependent SAXS measurements in combination with TEM and UV−vis spectroscopic investigations allow a more detailed mechanistic interpretation of the formation of gold nanotriangles in a multivesicular AOT/phospholipid template phase. In the first period spherical nanoparticles are formed at the vesicle surface, especially at the junction points inside of the multivesicular vesicles, which build up soft aggregates in the presence of AOT. In the second time period at their peripheries nanotriangles are formed, which grow up via an Ostwald ripening-based mechanism 16 times faster in the lateral than in the vertical direction. Due to the adsorption of symmetry-breaking components, i.e., AOT and the polyampholyte PalPhBisCarb, on the {111} facets and the confinement of the coral-like structures the growth in vertical direction is hindered. Therefore, the platelet thickness is leveled off at 7.1 nm and the diameter at 23 nm. To verify the adsorption behavior of AOT, phospholipon, and PalPhBisCarb on {111} gold facets in more detail, MD simulations are in progress. Finally, the aggregates decompose into spherical particles and very stable flat nanotriangles, which can be separated by a polyelectrolyte/micelle depletion flocculation.[4] A procedure to synthesize only nanotriangles in a one-step process in a vesicular template phase is still missing. Recently, we have shown that ultrasound treatment can induce a transformation into a tubular network structure.[7] However, the yield of gold nanotriangles does not exceed 30% by varying the temperature or the kinetic procedure of adding the components.[37]

AUTHOR INFORMATION

Corresponding Author

*E-mail: koetz@uni-potsdam.de. Phone: +49 331 977 5220.

Notes

The authors declare no competing financial interest.

ACKNOWLEDGMENTS

Financial support from the German Research Foundation (KO 1387/14-1) is gratefully acknowledged.

REFERENCES

(1) Eustis, S.; El-Sayed, M. A. Why gold nanoparticles are more precious than pretty gold: Noble metal surface plasmon resonance and its enhancement of the radiative and nonradiative properties of nanocrystals of different shapes. *Chem. Soc. Rev.* **2006**, *35*, 209−217.

(2) Shankar, S. S.; Rai, A.; Ahmad, A.; Sastry, M. Controlling the Optical Properties of Lemongrass Extract Synthesized Gold Nanotriangles and Potential Application in Infrared-Absorbing Optical Coatings. *Chem. Mater.* **2005**, *17*, 566−572.

(3) Lohse, S. E.; Murphy, C. J. The Quest for Shape Control: A History of Gold Nanorod Synthesis. *Chem. Mater.* **2013**, *25*, 1250−1261.

(4) Liebig, F.; Sarhan, R. M.; Prietzel, C.; Reinecke, A.; Koetz, J. Green" gold nanotriangles: synthesis, purification by polyelectrolyte/micelle depletion flocculation and performance in surface-enhanced Raman scattering. *RSC Adv.* **2016**, *6*, 33561−33568.

(5) Scarabelli, L.; Coronado-Puchau, M.; Giner-Casares, J. J.; Langer, J.; Liz-Marzan, L. M. Monodisperse Gold Nanotriangles: Size Control, Large-Scale Self-Assembly, and Performance in Surface-Enhanced Raman Scattering. *ACS Nano* **2014**, *8*, 5833−5842.

(6) Rai, A.; Singh, A.; Ahmad, A.; Sastry, M. Role of Halide Ions and Temperature on the Morphology of Biologically Synthesized Gold Nanotriangles. *Langmuir* **2006**, *22*, 736−741.

(7) Schulze, N.; Prietzel, C.; Koetz, J. Polyampholyte-mediated synthesis of anisotropic gold nanoplatelets. *Colloid Polym. Sci.* **2016**, *294*, 1297−1304.

(8) Oldenburg, S. J.; Jackson, J. B.; Westcott, S. L.; Halas, N. J. Infrared extinction properties of gold nanoshells. *Appl. Phys. Lett.* **1999**, *75*, 2897−2895.

(9) Daniel, M. C.; Astruc, D. Gold nanoparticles: assembly, supramolecular chemistry, quantum-size-related properties, and applications toward biology, catalysis, and nanotechnology. *Chem. Rev.* **2004**, *104*, 293−346.

(10) Loo, C.; Lin, A.; Hirsch, L.; Lee, M. H.; Barton, J.; Halas, N.; West, J.; Drezek, R. Nanoshell-enabled photonics-based imaging and therapy of cancer. *Technol. Cancer Res. Treat.* **2004**, *3*, 33−40.

(11) Gao, J.; Bender, C. M.; Murphy, C. J. Dependence of Gold Nanorod Aspect Ratio on the Nature of the Directing Surfactant in Aqueous Solution. *Langmuir* **2003**, *19*, 9065−9070.

DOI: 10.1021/acs.langmuir.6b02662
Langmuir 2016, 32, 10928−10935

(12) Xia, Y.; Xiong, Y.; Lim, B.; Skrabalak, S. E. Shape-controlled synthesis of metal nanocrystals: simple chemistry meets complex physics? *Angew. Chem., Int. Ed.* **2009**, *48*, 60−103.
(13) Jana, N. R.; Gearheart, L.; Murphy, C. J. Seeding Growth for Size Control of 5−40 nm Diameter Gold Nanoparticles. *Langmuir* **2001**, *17*, 6782−6786.
(14) Lohse, S. E.; Burrows, N. D.; Scarabelli, L.; Liz-Marzan, L. M.; Murphy, C. J. Anisotropic Noble Metal Nanocrystal Growth: The Role of Halides. *Chem. Mater.* **2014**, *26*, 34−43.
(15) Kim, J.; Hong, S.; Jang, H.-J.; Choi, Y.; Park, S. Influence of iodide ions on morphology of silver growth on gold hexagonal nanoplates. *J. Colloid Interface Sci.* **2013**, *389*, 71−76.
(16) Hong, S.; Acapulco, J. A. I.; Jang, H.-J.; Kulkarni, A. S.; Park, S. Kinetically Controlled Growth of Gold Nanoplates and Nanorods via a One-Step Seed-Mediated Method. *Bull. Korean Chem. Soc.* **2014**, *35*, 1737−1742.
(17) Kasture, M.; Sastry, M.; Prasad, B. L. V. Halide ion controlled shape dependent gold nanoparticle synthesis with tryptophan as reducing agent: Enhanced fluorescent properties and white light emission. *Chem. Phys. Lett.* **2010**, *484*, 271−275.
(18) Scott, R. W.; Wilson, O. M.; Crooks, R. M. Synthesis, characterization, and applications of dendrimer-encapsulated nanoparticles. *J. Phys. Chem. B* **2005**, *109*, 692−704.
(19) Ding, W.; Lin, J.; Yao, K.; Mays, J. W.; Ramanathan, M.; Hong, K. Building triangular nanoprisms from the bottom-up: a polyelectrolyte micellar approach. *J. Mater. Chem. B* **2013**, *1*, 4212−4216.
(20) Robertson, D.; Tiersch, B.; Kosmella, S.; Koetz, J. Preparation of crystalline gold nanoparticles at the surface of mixed phosphatidylcholine-ionic surfactant vesicles. *J. Colloid Interface Sci.* **2007**, *305*, 345−351.
(21) Köth, A.; Appelhans, D.; Prietzel, C.; Koetz, J. Asymmetric gold nanoparticles synthesized in the presence of maltose-modified poly(ethyleneimine). *Colloids Surf., A* **2012**, *414*, 50−56.
(22) Fechner, M.; Koetz, J. Potentiometric Behavior of Polyampholytes Based on N,Ń-diallyl-N,Ń-dimethylammonium Chloride and Maleamic Acid Derivatives. *Macromol. Chem. Phys.* **2011**, *212*, 2691−2699.
(23) Orthaber, D.; Bergmann, A.; Glatter, O. SAXS experiments on absolute scale with Kratky systems using water as a secondary standard. *J. Appl. Crystallogr.* **2000**, *33*, 218−225.
(24) Bressler, I.; Kohlbrecher, J.; Thunemann, A. F. SASfit: a tool for small-angle scattering data analysis using a library of analytical expressions. *J. Appl. Crystallogr.* **2015**, *48*, 1587−1598.
(25) Bienert, R.; Emmerling, F.; Thunemann, A. F. The size distribution of 'gold standard' nanoparticles. *Anal. Bioanal. Chem.* **2009**, *395*, 1651−1660.
(26) Bujan, M.; Sikiric, M.; Filipovic-Vincekovic, N.; Vdovic, N.; Garti, N.; Füredi-Milhofer, H. Effect of Anionic Surfactants on Crystal Growth of Calcium Hydrogen Phosphate Dihydrate. *Langmuir* **2001**, *17*, 6461−6470.
(27) Du, J.; Tang, Y.; Lewis, A. L.; Armes, S. P. pH-sensitive vesicles based on a biocompatible zwitterionic diblock copolymer. *J. Am. Chem. Soc.* **2005**, *127*, 17982−17983.
(28) Genc, R.; Clergeaud, G.; Ortiz, M.; O'Sullivan, C. K. Green Synthesis of Gold Nanoparticles Using Glycerol-Incorporated Nanosized Liposomes. *Langmuir* **2011**, *27*, 10894−10900.
(29) Schulze, N.; Appelhans, D.; Tiersch, B.; Koetz, J. Morphological transformation of vesicles into tubular structures by adding polyampholytes or dendritic glycopolymers. *Colloids Surf., A* **2014**, *457*, 326−332.
(30) Harada, M.; Tamura, N.; Takenaka, M. Nucleation and Growth of Metal Nanoparticles during Photoreduction Using In Situ Time-Resolved SAXS Analysis. *J. Phys. Chem. C* **2011**, *115*, 14081−14092.
(31) Boistelle, R.; Astier, J. P. Crystallization mechanisms in solution. *J. Cryst. Growth* **1988**, *90*, 14−30.
(32) Lifshitz, I. M.; Slyozov, V. V. The kinetics of precipitation from supersaturated solid solution. *J. Phys. Chem. Solids* **1961**, *19*, 35−50.
(33) Wagner, C. Theory of precipitate change by redis- solution (Ostwald ripening). *Z. Elektrochem.* **1961**, *65*, 581−591.
(34) Harada, M.; Kizaki, S. Formation Mechanism of Gold Nanoparticles Synthesized by Photoreduction in Aqueous Ethanol Solutions of Polymers Using In Situ Quick Scanning X-ray Absorption Fine Structure and Small-Angle X-ray Scattering. *Cryst. Growth Des.* **2016**, *16*, 1200−1212.
(35) Lofton, C.; Sigmund, W. Mechanism Controlling Crystal Habits of Gold and Silver Colloids. *Adv. Funct. Mater.* **2005**, *15*, 1197−1208.
(36) Zeng, J.; Xia, X.; Rycenga, M.; Henneghan, P.; Li, Q.; Xia, Y. Successive Deposition of Silver on Silver Nanoplates: Lateral versus Vertical Growth. *Angew. Chem.* **2011**, *123*, 258−263.
(37) Schulze, N.; Koetz, J. Kinetically controlled growth of gold nanotriangles in a vesicular template phase by adding a strongly alternating polyampholyte. *J. Dispersion Sci. Technol.* **2016**, DOI: 10.1080/01932691.2016.1220318.

DOI: 10.1021/acs.langmuir.6b02662
Langmuir 2016, 32, 10928−10935